# Unveiling AGN outflows: [O III] Outflow detection rates and correlation with low-frequency radio emission

Escott, E.L.; Morabito, L.K.; Scholtz, J.; Hickox, R.C.; Harrison, C.M.; Alexander, D.M.; ... ; Kolwa, S.

**Citation**
Escott, E. L., Morabito, L. K., Scholtz, J., Hickox, R. C., Harrison, C. M., Alexander, D. M., ... Kolwa, S. (2025). Unveiling AGN outflows: [O III] Outflow detection rates and correlation with low-frequency radio emission. *Monthly Notices Of The Royal Astronomical Society, 536*(2), 1166-1179. doi:10.1093/mnras/stae2645

| | |
|---|---|
| Version: | Publisher's Version |
| License: | Creative Commons CC BY 4.0 license |
| Downloaded from: | https://hdl.handle.net/1887/4288642 |

**Note:** To cite this publication please use the final published version (if applicable).

Monthly Notices of the ROYAL ASTRONOMICAL SOCIETY

MNRAS **536,** 1166–1179 (2025) https://doi.org/10.1093/mnras/stae2645
Advance Access publication 2024 November 27

# Unveiling AGN outflows: [O III] outflow detection rates and correlation with low-frequency radio emission

Emmy L. Escott [1]★ Leah K. Morabito [1,2]★ Jan Scholtz,[3] Ryan C. Hickox,[4] Chris M. Harrison [5] David M. Alexander,[1] Marina I. Arnaudova [6] Daniel J. B. Smith,[6] Kenneth J. Duncan [7] James Petley,[1,8] Rohit Kondapally [7] Gabriela Calistro Rivera [9] and Sthabile Kolwa[10]

[1]*Centre for Extragalactic Astronomy, Department of Physics, Durham University, South Road, Durham DH1 3LE, UK*
[2]*Institute for Computational Cosmology, Department of Physics, Durham University, South Road, Durham DH1 3LE, UK*
[3]*Kavli Institute for Cosmology, University of Cambridge, Madingley Road, Cambridge CB3 OHA, UK*
[4]*Department of Physics and Astronomy, Dartmouth College, 6127 Wilder Laboratory, Hanover, NH 03755, USA*
[5]*School of Mathematics, Statistics and Physics, Newcastle University, Newcastle NE1 7RU, UK*
[6]*Centre for Astrophysics Research, University of Hertfordshire, College Lane, Hatfield AL10 9AB, UK*
[7]*Institute for Astronomy, University of Edinburgh Royal Observatory, Blackford Hill, Edinburgh EH9 3HJ, UK*
[8]*Leiden Observatory, Leiden University, PO Box 9513, NL-2300 RA Leiden, the Netherlands*
[9]*European Southern Observatory, Karl-Schwarzschild-Straße 2, D-85748 Garching bei München, Germany*
[10]*Physics Department, University of Johannesburg, 5 Kingsway Ave, Rossmore, Johannesburg 2092, South Africa*

Accepted 2024 November 21. Received 2024 October 15; in original form 2024 January 26

## ABSTRACT

Some active galactic nuclei (AGN) host outflows which have the potential to alter the host galaxy's evolution (AGN feedback). These outflows have been linked to enhanced radio emission. Here, we investigate the connection between low-frequency radio emission using the international LOw Frequency ARray (LOFAR) telescope and [O III] λ5007 ionized gas outflows using the Sloan Digital Sky Survey. Using the LOFAR Two-metre Sky Survey (LoTSS) Deep Fields, we select 198 AGN with optical spectra, 115 of which are detected at 144 MHz, and investigate their low-frequency radio emission properties. The majority of our sample do not show a radio excess when considering radio luminosity – star formation rate relationship, and are therefore not driven by powerful jets. We extract the [O III] λ5007 kinematics and remove AGN luminosity dependencies by matching the radio detected and non-detected AGN in $L_{6\,\mu m}$ and redshift. Using both spectral fitting and $W_{80}$ measurements, we find radio detected AGN have a higher outflow rate (67.2 ± 3.4 per cent) than the radio non-detected AGN (44.6 ± 2.7 per cent), indicating a connection between ionized outflows and the presence of radio emission. For spectra where there are two components of the [O III] emission line present, we normalize all spectra by the narrow component and find that the average broad component in radio detected AGN is enhanced compared to the radio non-detected AGN. This could be a sign of higher gas content, which is suggestive of a spatial relationship between [O III] outflows and radio emission in the form of either low-powered jets or shocks from AGN winds.

**Key words:** ISM: jets and outflows – galaxies: active – galaxies: jets – galaxies: kinematics and dynamics – quasars: emission lines – radio continuum: galaxies.

## 1 INTRODUCTION

A significant number of observational studies show that at the centre of almost every galaxy, there is a supermassive black hole (SMBH; Kormendy & Richstone 1992, 1995; Magorrian et al. 1998) and when a SMBH shows signs of accretion, it is known as an active galactic nucleus (AGN).Some of the most powerful objects in our Universe and the most powerful subclass of AGN, which are termed quasars, have the potential to emit a bolometric luminosity of $10^{48}$ ergs$^{-1}$ (see Alexander & Hickox 2012, for a review). The gravitational potential of an accreting SMBH can power intense phenomena (Antonucci 1993; Urry & Padovani 1995) which can expel vast amounts of gas out of the host galaxy.

The activity from the SMBH is believed to have a profound effect on the evolution of the galaxy, a process called AGN feedback, although our only evidence for this is indirect (Fabian 2012). We see in observational data that there is a correlation between the mass of the SMBH and global properties such as the velocity dispersion of the galaxy (Gebhardt et al. 2000; Merritt & Ferrarese 2001), which suggests the two are linked. Furthermore, cosmological simulations are unable to reproduce the observed universe without including AGN feedback providing heating effects from AGN in their models (Bower et al. 2006; Croton et al. 2006). AGN feedback can be enacted by powerful phenomena such as shocks induced by winds, ionized, and molecular outflows, and jets. However, despite indications that

★ E-mail: emily.l.escott@durham.ac.uk (ELE); leah.k.morabito@durham.ac.uk (LKM)

© 2024 The Author(s).
Published by Oxford University Press on behalf of Royal Astronomical Society. This is an Open Access article distributed under the terms of the Creative Commons Attribution License (https://creativecommons.org/licenses/by/4.0/), which permits unrestricted reuse, distribution, and reproduction in any medium, provided the original work is properly cited.

Downloaded from https://academic.oup.com/mnras/article/536/2/1166/7911849 by Universiteit Leiden - LUMC user on 30 January 2026

AGN impact how galaxies form and evolve, AGN feedback is still a major open area of research, with many questions waiting to be answered, such as which physical processes are the major cause of turbulent outflows in the interstellar medium (ISM) and how these outflows differ with galactic properties.

Processes that generate radio emission are often associated with AGN feedback. One channel is through the most powerful radio jets that commonly originate from AGN which have a much higher radio to optical flux density ratio (radio-loud AGN; Kellermann et al. 1989). Powerful radio jets are clearly seen to interact with their environments and host galaxies, for example by driving bulk outflows of ionized gas (e.g. Tadhunter & Tsvetanov 1989; Villar-Martín, Binette & Fosbury 1999; Birzan et al. 2004). We see evidence for AGN feedback from these radio jets on large scale (∼100 kpc), for example from galaxy clusters (e.g. Gitti, Brighenti & McNamara 2012; McNamara & Nulsen 2012; Timmerman et al. 2022) where jets inflate radio lobes into the ISM producing X-ray cavities. On galactic scales, jets are associated with, for example disturbed emission line kinematics (e.g. Zakamska & Greene 2014; Speranza et al. 2023) or radio lobe expansion (Webster et al. 2021).

The radio emission from radio-loud AGN is likely due to a radio jet being present (Urry & Padovani 1995), on the other hand the origin of the radio emission in radio-quiet AGN remains unclear. The emission could be produced by low-powered jets, the corona, stellar winds or star formation (see Panessa et al. 2019, and references therein). Bonzini et al. (2015), Padovani et al. (2011), and Delvecchio et al. (2017) suggest the emission is due to star formation, however, other studies (e.g. White et al. 2015; Macfarlane et al. 2021; Calistro Rivera et al. 2024; Yue et al. 2024) propose that the radio emission from radio-quiet AGN is due to accretion activity rather than star formation. Moreover, Petley et al. (2022) connects the radio emission in broad absorption line quasars to the outflow properties, suggesting the radio emission may originate from AGN induced winds.

The [O III] λ5007 emission line is commonly used as a tracer for warm, ionized gas outflows. These outflows are firmly linked to radio properties, which makes studies of the connection between radio and [O III] a promising avenue for investigating AGN feedback. Rawlings et al. (1989) shows that the [O III] and radio luminosities are correlated in a sample of radio galaxies at $z\sim 0.5$. Mullaney et al. (2013) characterizes the [O III] λ5007 profiles of 24 264 optically selected AGN at $z\sim 0.4$ and links the most disturbed [O III] to being induced by compact radio cores rather than powerful radio jets. Using a sample of 129 uniformly selected radio AGN with $z< 0.23$, Kukreti et al. (2023) uses stacking analysis with Sloan Digital Sky Survey (SDSS) spectra to discover that radio AGN with a peak in their radio spectra drives a broader outflowing component in [O III] than radio AGN without a peak in their spectrum. In the more distant Universe, Nesvadba et al. (2017) present the [O III] λ5007 maps and kinematics for 33 $z> 2$ radio galaxies using Very Large Telescope/Spectrograph for INtegral Field Observations in the Near Infrared (VLT/SINFONI) imaging spectroscopy, finding complex gas kinematics in all sources and Zakamska et al. (2016) study the [O III] kinematics of red quasars at $z\sim 2.5$ using XSHOOTER on the VLT, discovering very broad and blueshifted [O III] emission lines. Extending to a sample of radio-quiet AGN, Jarvis et al. (2019) and Girdhar et al. (2022) show that jets drive biconical [O III] outflows with the jets strongly interacting at their termini with the ISM. Due to these links between radio emission and [O III] outflows, after identifying outflows, we can then compare the extracted kinematics to radio data and start to understand how the radio emission is linked to these outflows.

The [O III] λ5007 emission line is driven by both a gravitational and non-gravitational component. The gravitational component is dependent on the virial motion of the gas of the host galaxy, whereas if an outflow is present, this will produce a non-gravitational component which is commonly seen as the blueshifted shoulder (Greene & Ho 2005). Woo et al. (2016) suggest that the enhanced [O III] velocity dispersion seen with increasing radio luminosity is due to host galaxy properties. They report that the positive relation between [O III] velocity dispersion and $L_{1.4\,\mathrm{GHz}}$ becomes insignificant once normalized by the stellar velocity dispersion. However, more recently Ayubinia et al. (2023) show that radio activity does play a role in the enhancement of ionized gas kinematics after normalizing in stellar velocity dispersion, suggesting that radio activity yields an additional boost to these outflows. It is still unclear how and to what extent radio emission is linked to the ionized outflows observed in the [O III] emission line.

The LOw Frequency ARray (LOFAR; Haarlem et al. 2013) has the potential to provide the answer. The LOFAR Two-metre Sky Survey (LoTSS; Shimwell et al. 2017, 2019, 2022) is an ongoing survey, which aims to cover the entire Northern hemisphere at a frequency of 144 MHz. With this data, 6 arcsec resolution imaging is possible with an average sensitivity of $\sim$70 μJy beam$^{-1}$. Due to LOFAR's wide field of view and high level of sensitivity, it is a powerful instrument to conduct deep field surveys. Alongside LoTSS there is also a data release for three deep fields: Lockman Hole, European Large Area Infrared Space Observatory Survey-North 1 (ELAIS-N1), and Boötes (Sabater et al. 2021; Tasse et al. 2021). The first deep fields data release reached sensitivities of 22, 20, and 30 μJy beam$^{-1}$, respectively, which before LoTSS was unprecedented at such low frequencies. To emphasize how deep this survey is, if LOFAR operated at the same $L_{1.4\mathrm{GHz}}$ frequency as the VLA (Very Large Array), then Boötes and Lockman would have sensitivities (assuming a typical synchrotron spectral index of −0.7) of 6 and 5 μJy beam$^{-1}$, respectively. Comparatively the VLA-COSMOS Deep Survey (Schinnerer et al. 2004, 2007) reaches sensitives between 7 and 15 μJy beam$^{-1}$ at this frequency, but only covers $\sim$2 deg$^2$ of the sky, whereas the LoTSS Deep Fields combined cover a much larger field of view of $\sim$27 deg$^2$, providing bigger samples for statistical studies. With such deep data at low frequencies we can probe significantly faint radio emission produced predominately by synchrotron emission, without susceptibility to free–free contamination, to further our understanding of the radio sky and large samples of low radio luminosity AGN can be obtained and studied.

This is the first of two papers to help us further understand the link between [O III] and low-frequency radio emission. Within this first paper, we fit the [O III] emission line to investigate [O III] kinematics of AGN within the LoTSS Deep Fields to investigate the link between radio emission and [O III] kinematics for a well-defined sample of AGN. This allows us to compare the [O III] properties between AGN detected within the LoTSS Deep Fields and AGN that are not detected. For the second paper, we will fully utilize the capabilities of LOFAR by studying the radio morphologies of these AGN at subarcsec resolution using images from Sweijen et al. (2022), de Jong et al. (), and Escott et al., in preparation. This will allow us to understand the radio emission of these AGN down to subgalactic scales and link these morphologies to [O III] kinematics and outflows.

In this paper, we first summarize the data and sample selection in Section 2. In Section 3, we outline the spectral fitting procedure and treatment of [O III] outflows. We present the results of this paper in Section 4 and then the discussion and conclusions are in Sections 5 and 6, respectively. In this work, we assume a Wilkinson Microwave Anisotropy Probe 9 (WMAP9) cosmology (Hinshaw et al. 2013) with $H_0 = 69.32$ km s$^{-1}$Mpc$^{-1}$, $\Omega_m = 0.287$, and $\Omega_\Lambda = 0.713$.

Downloaded from https://academic.oup.com/mnras/article/536/2/1166/7911849 by Universiteit Leiden - LUMC user on 30 January 2026

## 2 DATA

### 2.1 LoTSS Deep Fields

We focus on all three LoTSS Deep Fields: ELAIS-N1, Lockman Hole, and Boötes (Sabater et al. 2021; Tasse et al. 2021) (∼7.15, ∼10.7, and ∼9.5 deg$^2$, respectively). We use the Deep Fields in LoTSS due to Lockman Hole and ELAIS-N1 benefiting from high-resolution images presented in Sweijen et al. (2022) and de Jong et al. (2024). A similar image will soon be available for the Boötes field (Escott et al., in preparation). In a follow-up paper, we will use these high-resolution images to further understand the link between [O III] and radio emission. Furthermore, we use these Deep Fields because the low-frequency radio emission is ∼4 times deeper than the standard DR2 LoTSS images meaning we can probe a new parameter space, down to fainter radio luminosities. These fields also provide excellent ancillary data. The observations are at a central frequency of 144 MHz for both Boötes and Lockman Hole, and 146 MHz for ELAIS-N1, with a total integration time of 80 h for Boötes, 112 h for Lockman Hole, and 164 h for ELAIS-N1. Boötes has a central sensitivity of 32 μJy, for Lockman Hole the central sensitivity is 22 μJy, and 20 μJy for ELAIS-N1, with the noise increasing towards the edge of the images and bright sources.

#### *2.1.1 Multiwavelength data*

The multiwavelength catalogue for the LoTSS Deep Fields is described in Kondapally et al. (2021) but we summarize the data here. The LoTSS Boötes Deep Field catalogue is cross-matched with the National Optical Astronomy Observatory (NOAO) Deep Wide Field Survey (NDWFS; Jannuzi & Dey 1999) which are detected in the I and Infrared Array Camera (IRAC) 4.5 μm bands (Brown et al. 2007, 2008) where Brown et al. (2007) combines 15 multiwavelength bands between 0.14 and 24 μm from various surveys with Point Spread Function (PSF) matched aperture photometry.The catalogue also contains: ultraviolet (UV) from Galaxy Evolution Explorer (GALEX) surveys, near-infrared (NIR) from Gonzalez et al. (2010), as well as mid-infrared (MIR) from the *Spitzer* Deep Wide Field Survey (SDWFS; Ashby et al. 2009), and far-infrared (FIR) data from High efficiency and resolution Mercator Echelle Spectrograph (HerMES) and Multi-band Imaging Photometer (MIPS).

The multiwavelength catalogue for Lockman Hole has the largest area of the Deep Fields covered in Kondapally et al. (2021) and has wavelength coverage between 0.15 and 500 μm. The MIR data uses the IRAC instrument on the *Spitzer* Space Telescope (Werner et al. 2004), more specifically, *Spitzer* Wide-Area Infrared Extragalactic Survey (SWIRE; Lonsdale et al. 2003) and the *Spitzer* Extragalactic Representative Volume Survey (SERVS; Mauduit et al. 2012). For more details on both fields consult Kondapally et al. (2021).

ELAIS-N1 has the same wavelength coverage as Lockman Hole, 0.15–500 μm, and the MIR data also uses SWIRE and SERVS. The UV data are from the Deep Imaging Survey (DIS) using GALEX (Martin et al. 2005; Morrissey et al. 2007), the NIR data are from the UK Infrared Deep Sky Survey (UKIDISS), Deep Extragalactic Survey (DXS) DR10 (Lawrence et al. 2007), and FIR from HerMES and MIPS. The optical data come from the Panoramic Survey Telescope and Rapid Response System (Pan-STARRS-1; Kaiser et al. 2010) and Hyper Suprime-Cam Subaru Strategic Program (HSC-SSP; Aihara et al. 2018).

We use derived properties for the radio detected AGN such as star formation rates (SFRs) and stellar masses from the catalogue described in Best et al. (2023). The authors use spectral energy distribution (SED) fitting to calculate these derived properties. These SEDs span from the UV to FIR and from these the authors obtain a consensus SFR and consensus stellar mass. When an AGN component is present, this is accounted for within the SED fitting code.

### 2.2 Optical SDSS spectra

In this work, we use optical spectra from the Sloan Digital Sky Survey (SDSS). To identify these spectra, we use two catalouges: the SDSS DR16 Quasar catalogue (Lyke et al. 2020) and a broad-line AGN catalogue from (Liu et al. 2019). The DR16 Quasar catalogue (Lyke et al. 2020) consists of 750 414 spectroscopically confirmed quasars across 9376 deg$^2$. The broad-line AGN catalogue, Liu et al. (2019), is composed of 14 584 AGN at $z < 0.35$, identified by the width of Balmer emission lines, particularly H$\alpha$. Lyke et al. (2020) includes all quasar sources classified by SDSS I, II and III, while the catalogue from Liu et al. (2019) identifies broad-line AGN among SDSS DR7 sources. The SDSS spectra associated with these catalogues are from the original SDSS spectrograph or the newer Baryon Oscillation Spectroscopic Survey (BOSS) instrument. The wavelength coverage for the original spectrograph is 3800–9200 Å, compared with the improved BOSS coverage of 3650–10400 Å with a spectroscopic resolution of 1500 at 3800 Å, and 2500 at 9000 Å. These catalogues together fill the redshift–luminosity space with AGN at lower redshifts (Liu et al. 2019) and quasars at higher redshifts (Lyke et al. 2020). We use these two catalogues as the basis to select our sample as described in Section 2.3.

### 2.3 Sample selection

To construct our sample, we first remove any sources in Liu et al. (2019) that are duplicated within Lyke et al. (2020) and then apply Multi-Order Coverage Maps (MOCs) of the respective Deep Fields (Kondapally et al. 2021) so that radio data from the LoTSS Deep Fields (see Section 2.1) are available. Bright sources may also affect the data quality of some areas of the sky. We therefore apply starmasks[1] to each field to remove this unreliable data.

The next step is to ensure [O III] spectral information is accessible so we can analyse the emission line's kinematics. We remove AGN from our sample with $z > 0.83$, to ensure we can analyse [O III] equally across the AGN. This leaves 332 AGN remaining.

The spectra for seven sources could not be downloaded from the SDSS spectral search and upon manually searching their plate details it appeared these spectra had no spectral lines which indicates potential incorrect classification, hence we remove these from our sample. We remove an additional two AGN in Boötes. One is removed because upon visual inspection we find that [O III] and H$\beta$ are double-peaked emission lines, which can be characteristic of dual AGN (Zhou et al. 2004). Very Long Baseline Interferometry (VLBI) imaging at 1.7 and 5 GHz from Frey et al. (2012) further supports that this object is a dual AGN. For the other source, we choose to discard this due to lack of emission lines in the optical spectrum, including [O III]. It is possible that this is a misidentification or this AGN could be an optically quiescent quasar (Greenwell et al. 2021), which maybe obscured due to a 'cocooned' phase of the NLR (narrow line region). To confirm this, we would require the infrared (IR) spectrum to see if there is strong [O III] emission present and an X-ray observation to see if the emission can be identified as an AGN.

[1]The MOCs and starmasks are available at https://lofar-surveys.org/deepfields.html.



Downloaded from https://academic.oup.com/mnras/article/536/2/1166/7911849 by Universiteit Leiden - LUMC user on 30 January 2026

In the Lockman Hole field, we remove three AGN after attempting to fit the spectra. It became clear there is not enough information in the spectral window to provide robust fits and therefore we remove the sources from the sample. This leaves a sample of 320 AGN, 100 in Boötes, 137 in Lockman Hole, and 83 in ELAIS-N1.

The results of this paper rely on extracting information from spectra, so we implement a signal to noise (SNR) cut of 5, where the signal is taken from the continuum subtracted [O III] λ5007, while the noise is measured from two line-free spectral windows at 5040–5060 Å and 4760–4840 Å. We also test SNR cuts of 3 and 10 and find the results remain consistent, therefore we use a cut of 5 as a balance between high SNR and sample size. The mean SNR of the 320 AGN is 15.32 and using a cut of 5, we reduce the sample from 320 AGN to 217 AGN with a similar percentage of sources removed in each field. The SNR cut is necessary because, as discussed in Section 3.1, distinguishing between broad, weak outflows, and noise can be difficult for low-SNR sources.

To further ensure that any [O III] emission is real and not noise, we incorporate a cut which removes AGN which have a very broad narrow component fitted to [O III], where the peak of this narrow component is not significantly higher than the RMS (root mean squared) noise. If an AGN has a single component with a FWHM (full width at half-maximum) greater than 850 km $s^{-1}$ and the peak of the fitted component is less than 5 times the RMS of [O III], we remove these sources. This leaves 208 AGN.

We cross-match all 208 AGN with the optical and IR catalogues from Kondapally et al. (2021) using a search radius of 2 arcsec. We then ensure that MIR data are available for all of these sources which we can use as a proxy for AGN luminosity as described in Section 2.4. We discover that two sources (105057.30+593214.4 and 105902.18+584008.2) do not contain channel 3 and/or channel 4 *Spitzer* information and therefore, we are unable to conduct the matching process described in Section 2.4 and hence we remove these two sources from our sample. This leaves 206 AGN.

As part of the SDSS targeting procedure, in DR16Q many AGN are targeted because they are detected within 1 arcsec of a Faint Images of the Radio Sky at Twenty-one centimeters (FIRST) radio source, which could provide a radio-biased sample. We therefore remove eight sources with either a `QSO_EBOSS_FIRST`, `QSO1_EBOSS_FIRST`, or `QSO_FIRST_BOSS` flag, all of which are located in Boötes.

This leaves us with a final sample of 198 AGN. 90 reside in Lockman, 55 in Boötes, and 53 in ELAIS-N1.

#### 2.3.1 *Radio properties of the sample*

The multiwavelength catalogue from Kondapally et al. (2021) has already been cross-matched with the LoTSS data, providing radio information. As mentioned previously, the flux limits for the three Deep Fields are different. There is only one 5$\sigma$ source in Lockman Hole and another in ELAIS-N1 which is below the flux limit in the Boötes field. We therefore move these sources (ILTJ104811.63+591047.6 and ILTJ160946.89+550533.3) from the radio detected to radio non-detected population to provide an effectively consistent flux limit for the sample, but note that this does not change the results. We find that 115 sources have a LoTSS detection: 33 in Boötes, 55 in Lockman Hole, and 27 in ELAIS-N1. This leaves 83 AGN without a detection; 22 in Boötes, 26 in ELAIS-N1, and 35 in Lockman Hole.

We calculate the 144 MHz $k$-corrected luminosity using the spectral index, $\alpha$ (where $S_\nu \propto \nu^{-\alpha}$), assuming a typical synchrotron spectral index of $\alpha = 0.7$ (Klein, Lisenfeld & Verley 2018) and use the spectroscopic redshift from SDSS. For the radio non-detected AGN, we present upper limits calculated using the median value of an aperture with radius 3 arcsec from the RMS map of the relevant field[2] to ensure any possible emission is captured.

The final catalogue of the 198 AGN is available on VizieR CDS (Strasbourg astronomical Data Center), containing both optical and radio data, the fitting results described in Section 3.1 will be available upon request.

### 2.4 $L_{6\,\mu m}$–$z$ matching

Differences seen in [O III] between our radio detected and non-detected AGN could be driven by a luminosity bias. The MIR luminosity at 6 μm, $L_{6\,\mu m}$, is a popular tracer for AGN bolometric luminosity (Richards et al. 2006) because UV emission produced by the central AGN is absorbed by dust from the torus or NLR and gets re-emitted with MIR wavelengths, providing an orientation-free proxy for the AGN luminosity. Therefore $L_{6\,\mu m}$ can be used to remove an intrinsic luminosity bias between populations. We adopt a common method to match the populations in $L_{6\,\mu m}$ and redshift (e.g. Rosario et al. 2020; Andonie et al. 2022; Fawcett et al. 2023). We calculate $L_{6\,\mu m}$ for AGN within Boötes using the interpolated aperture and extinction-corrected flux densities from channel 3 (5.8 μm) and channel 4 (8 μm) of the *Spitzer* Deep, Wide-Field Survey (SDWFS; Ashby et al. 2009), and for Lockman Hole, as well as ELAIS-N1, we use the SWIRE (Lonsdale et al. 2003) fluxes, which are both included in Kondapally et al. (2021). To begin the matching process we start with the radio non-detected AGN (as this has the smaller population), and then we randomly select from the radio detected population so that each radio non-detected AGN has an equivalent radio detected AGN. We set the tolerance to be $\Delta z = 0.06$ and $\Delta \log L_{6\,\mu m} = 0.3$.

In Fig. 1, we see both the total sample without any matching alongside the closest matched population, where starting from the radio non-detected AGN, the closest radio detected AGN has been matched to said radio non-detected AGN. This closest matched population contains 118 AGN in total, 59 radio detected and 59 radio non-detected and are indicated by coloured markers in Fig. 1. When considering all 198 AGN, we can see that the average $L_{6\,\mu m}$ is higher in the radio detected AGN. However, after matching, the distribution of $L_{6\,\mu m}$ and redshift is now similar for the two populations. To statistically quantify the differences between the populations from the closest matched population portrayed in Fig. 1, we perform a 2D Kolmogorov–Smirnov (KS) test after the populations are matched between the $L_{6\,\mu m}$ and redshift of the two populations using the public code NDTEST[3] and obtain a $p$-value of 0.61, confirming that the two populations are statistically indistinguishable.

## 3 [O III] EMISSION LINE PROFILES AND OUTFLOW IDENTIFICATION

### 3.1 Spectral fitting

To model the emission line profile of the [O III] emission line and identify outflows, we use the fitting module of QUBESPEC IFU analysis code[4] (Scholtz et al. 2021). We simultaneously fit the [O III] λλ4959,5007 and H$\beta$λ4861 emission lines and their neighbouring

[2]RMS maps are available at https://lofar-surveys.org/deepfields.html.
[3]Written by Zhaozhou Li, https://github.com/syrte/ndtest.
[4]Available at https://github.com/honzascholtz/Qubespec.



Downloaded from https://academic.oup.com/mnras/article/536/2/1166/7911849 by Universiteit Leiden - LUMC user on 30 January 2026

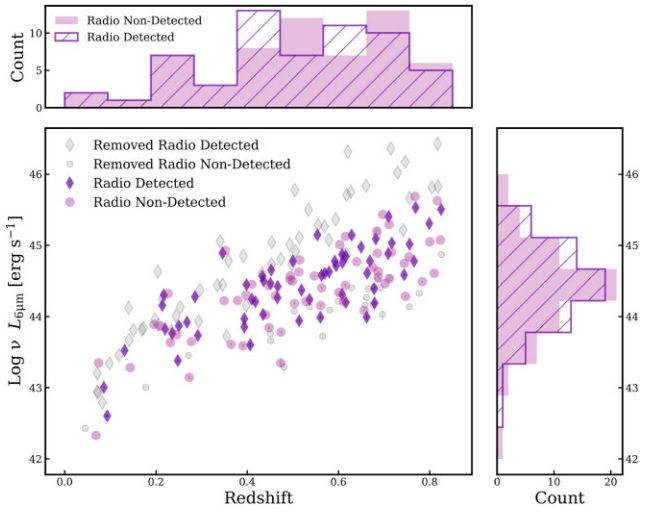


**Figure 1.** The $L_{6\,\mu m}$ and redshift relation of our radio and radio non-detected populations. The coloured markers show one iteration from the 1000 trials to match a radio detected AGN (purple diamonds) in $L_{6\,\mu m}$ and redshift to a radio non-detected AGN (pink circles). The grey points represent the AGN which, in this iteration, are removed as these are unmatched, with diamonds portraying the radio detected AGN, and circles for the radio non-detected AGN. The top histogram conveys the redshift distribution and the right histogram is the distribution of $L_{6\,\mu m}$. The hashed purple histogram is the radio detected AGN and the pink solid histogram are the radio non-detected AGN, showing they present similar distributions.

continuum between λ4800 and λ5100 Å. To describe emission line profiles, each line is modelled with one or two Gaussian components, with the line centroids, FWHM and fluxes (normalization) as free parameters. In each case the continuum is well characterized by a power law with slope and normalization as a free parameters. For the [O III] λλ4959,5007 Å emission line doublet we simultaneously fit [O III] λ4959 Å and [O III] λ5007 Å, using the respective vacuum rest-frame wavelengths of 4960.3 Å and 5008.24 Å. For both the narrow component and broad component (where present), we tie the line widths and central velocities of the two lines and fix the [O III] λ5007/[O III] λ4959 flux ratio to be 2.99 (Dimitrijević et al. 2007). We initially fit the continuum, [O III], and H$\beta$ models.

As some of our targets are luminous Type-1 AGN, we need to take into consideration the Fe II emission, originating from close to the accretion disc. This emission originates from a series of blended faint Fe II transitions that can appear as subtle features in the continuum that can mimic faint [O III] broad components. If we detect a broad H$\beta$ component indicating a BLR (broad line region), we refit the spectra with all the models including the Fe II templates. We follow the approach of Kakkad et al. (2020) and use different templates: no Fe II template, Veron, BG92, and Tsuzuki. We take the Veron template from the works of Véron-Cetty, Joly & Véron (2004), which takes the spectrum of I Zw 1 and uses the intensities of the broad and narrow Fe II lines to create a Fe II template. BG92, Boroson & Green (1992), removes all emission lines from I Zw 1 that are not Fe II and creates a template from this information. Finally, Tsuzuki from Tsuzuki et al. (2006) obtains further spectral information for I Zw 1 and separates Fe II emission from Mg II λ2798 in order to create this template. In each case, these templates are fitted after convolving with a Gaussian profile with a width of 2000–6000 km s$^{-1}$ (Park et al. 2022). The free parameters for each template are Gaussian convolution width and flux normalization of the template.

We do not couple the width and redshifts of H$\beta$ to the [O III] as these emission lines can have different line profiles in luminous AGN such as the ones we are investigating in this work (Scholtz et al. 2020, 2021). Furthermore, our observations are not sensitive enough to detect the faint outflow component in H$\beta$. Instead, two Gaussian profiles describe the emission from the NLR and BLR regions (if present). The H$\beta$ and [O III] velocity offset range from −180 to 193 km s$^{-1}$ for our matched AGN.

We use the Bayesian Information Criterion (BIC) to assess the quality of the fit and select the model with the lowest BIC score as best representing the data. We find the best-fit parameters using a Markov Chain Monte Carlo (MCMC; Goodman & Weare 2010) method, implemented using the EMCEEPYTHON library (Foreman-Mackey et al. 2013). We set uniform priors in log space for the normalizations of the continuum, Gaussian profiles, and Fe II templates, for example the FWHM of the broad component of [O III] was set to 2000 km s$^{-1}$ and allowed to deviate between 500 km s$^{-1}$ above and below this value. The final parameters quoted in this paper are the 50th percentile of the posterior distribution with errors describing the 68 per cent confidence interval.

After visual inspection of the spectral fits which are deemed to have the best-fitting by their BIC values, we find that for several spectra, the model with the lowest BIC value did not have the best-fitting to [O III]. This is because we calculate the BIC value by considering the whole spectral window, i.e. including H$\beta$. We therefore visually inspect all spectra to ensure that we prioritize the fit to the [O III] emission line, rather than other emission lines such as H$\beta$ that are within the spectral window. Fig. 2 shows some example spectra.

To calculate the [O III] luminosity, we integrate the continuum-subtracted region between 4975 and 5030 Å. We then convert this to luminosity by using the distance modulus, using spectroscopic redshifts from SDSS. To calculate the error in the [O III] luminosity we take the inverse square root of the inverse variance from the SDSS spectral information. We then sum the errors in quadrature.

### 3.2 Identifying outflows

We identify an outflow if there is a second, blueshifted Gaussian fitted to [O III] λ5007. However, even if an outflow is present, it might not always appear as a second component, due to observational limitations. Therefore, we further make use of the non-parametric $W_{80}$ measurement of [O III] to identify outflows. $W_{80}$ is the velocity width containing 80 per cent of the flux, calculated using the 10th and 90th percentiles of the velocities ($v_{10}$ and $v_{90}$, respectively) of [O III] λ5007 with $W_{80} = v_{90} - v_{10}$. We define two subcategories of outflows following the definitions stipulated in Harrison et al. (2014). When one component is fitted to [O III], AGN with $W_{80} > 800$ km s$^{-1}$ definitely host an outflow, and AGN with 600 km s$^{-1} < W_{80} < 800$ km s$^{-1}$ are likely to be undergoing an outflow because the majority of the [O III] total flux would be due to the outflowing component which is common especially in high-luminosity AGN (e.g. Carniani et al. 2015; Kakkad et al. 2020). Applying these limits is necessary to ensure that the kinematics seen are due to outflowing gas rather than gas bounded by the NLR or produced by star formation. Therefore, we separate our sample into two categories of [O III] outflows with subcategories within them:

(i) Outflow present

  (a) [O III] fitted outflow – second, blueshifted Gaussian present
  (b) $W_{80}$ outflow – one Gaussian fitted with $W_{80} > 800$ km s$^{-1}$



Downloaded from https://academic.oup.com/mnras/article/536/2/1166/7911849 by Universiteit Leiden - LUMC user on 30 January 2026

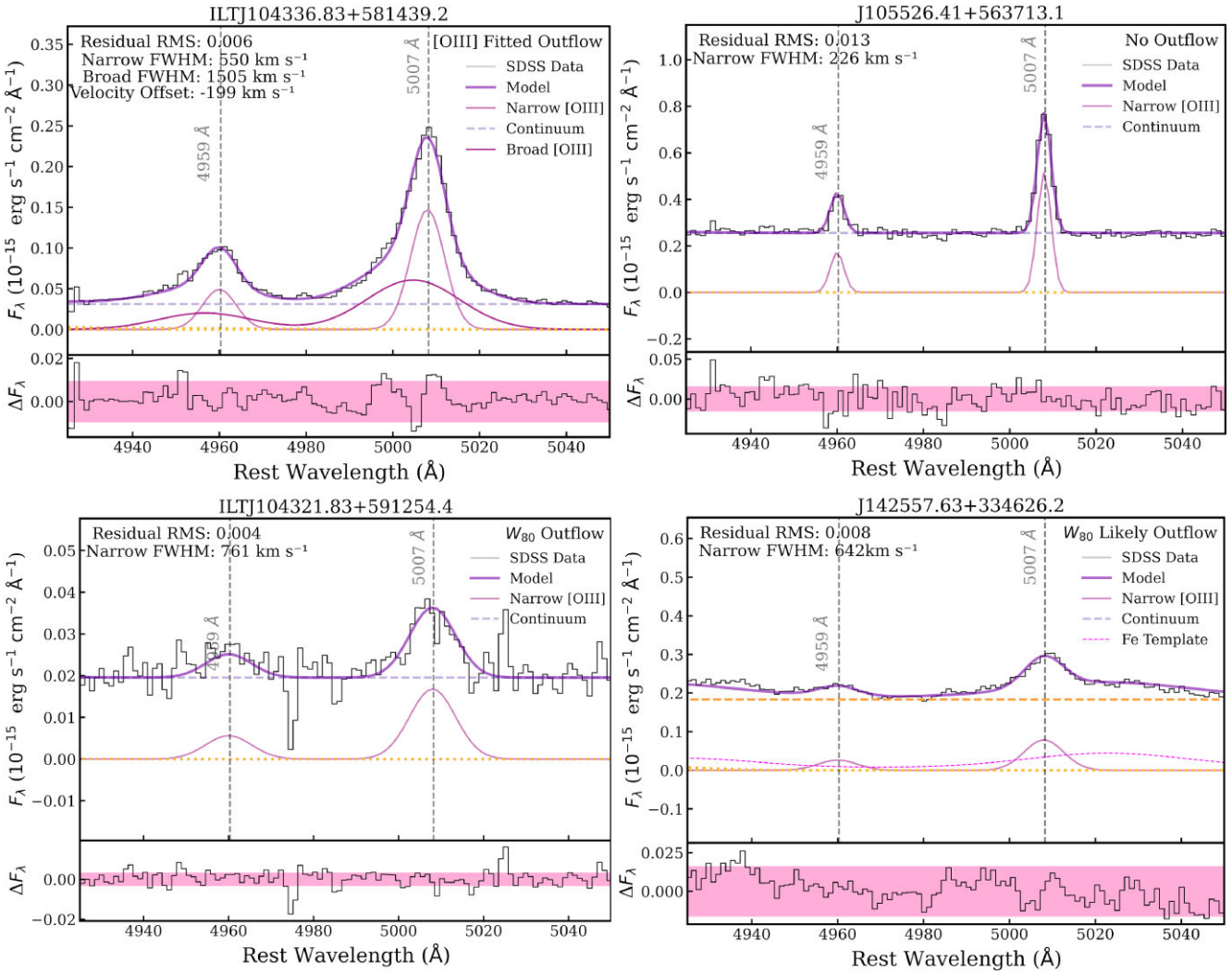


**Figure 2.** Example spectra for the four categories of the [O III] SDSS spectral fitting results. The top panel of each subplot represents the SDSS spectral data in black, alongside the MCMC fitting results. The dark purple solid lines shows the final MCMC fitting result. The pink Gaussians represent the narrow component to [O III] and the Gaussians in magenta, if plotted, is the broad component of [O III] which implies an outflow is occurring. The light pink dashed lines, where present, show the Fe II template used when modelling the data and finally the grey or yellow dashed lines shows the continuum. The lower panel of each subplot shows the residuals of the fit of the model to the SDSS data. The pink shaded region corresponds to RMS $1\sigma$ region, calculated over the full spectral range of the model. The titles of the radio detected AGN are the LoTSS source name of these AGN and start with ILTJ, the titles for the radio non-detected AGN are the SDSS name and they begin with J. Starting top left and going clockwise, the outflow groups of these AGN are [O III] fitted outflow, no outflow, $W_{80}$ outflow, and $W_{80}$ likely outflow.

(c) $W_{80}$ likely outflow – one Gaussian fitted with 600 km s$^{-1}$ $< W_{80} <$ 800 km s$^{-1}$.

(ii) No outflow – one Gaussian fitted with $W_{80} <$ 600 km s$^{-1}$.

An example of spectra showing each of these categories can be seen in Fig. 2, where the top left panel shows an [O III] fitted outflow, and the bottom left panel presents a $W_{80}$ outflow, bottom right panel a $W_{80}$ likely outflow, and top right panel an AGN with no outflow.

### 3.3 Stacking

To help visualize the average proportions of the [O III] emission line profile, we stack the radio detected population and radio non-detected populations separately within our matched subsample. As we are most interested in comparing the outflow properties of radio detected AGN to radio non-detected AGN, we first normalize each individual spectra by both their continuum as well as the peak of the narrow component of [O III] and then stack these normalized spectra. By normalizing the narrow component, we can directly compare the relative broad component in each stack. We use the stacking code presented in Arnaudova et al. (2024). In the observed frame, we first correct the spectra for Galactic extinction by using the recalibrated reddening data from Schlegel, Finkbeiner & Davis (1998), along with the Milky Way reddening curve from Fitzpatrick (1999). Then, all spectra are shifted to the rest frame by using the spectroscopic redshifts as measured from [O III] and are resampled on to a common wavelength grid, with a channel width of 1 Å using the SPECTRES: simple spectral resampling tool (Carnall 2017). In order to perform the stacking procedure, we take the median of each of the spectra and normalize them by subtracting the median and then dividing by the peak of [O III], where the median is computed at the reddest possible end of the area where all spectra populate the grid. A median stack is

Downloaded from https://academic.oup.com/mnras/article/536/2/1166/7911849 by Universiteit Leiden - LUMC user on 30 January 2026

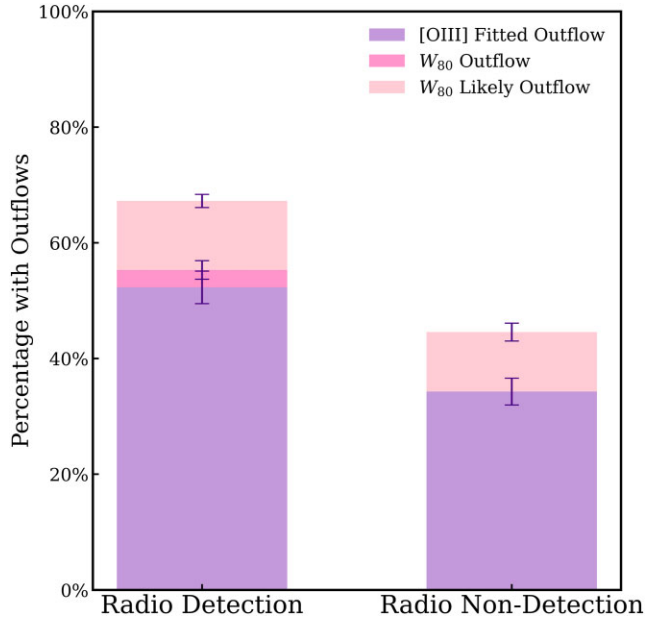


**Figure 3.** The stacked bar chart represents the average outflow detection rates from all 1000 iterations of randomly matching the radio detected AGN to the radio non-detected AGN. The light pink bar showing the $W_{80}$ likely outflows, the darker pink is the $W_{80}$ outflows, and the purple is the [O III] fitted outflows. For the radio detected AGN, 52.3 ± 2.8 per cent have an [O III] fitted outflow, 3.0 ± 1.6 per cent have $W_{80}$ outflows, 11.9 ± 1.1 per cent $W_{80}$ likely outflow, and 32.8 ± 2.5 per cent showing no signs of an outflow. In the same order the results for the radio non-detected AGN are, 34.3 ± 2.3 per cent, 0.0 ± 0.0 per cent, 10.3 ± 1.5 per cent, and 55.4 ± 2.4 per cent.

then performed where the associated uncertainties are bootstrapped. To ensure that the uncertainties are not underestimated, and that spectral features have not impacted the normalization, an additional simulation is performed (see Arnaudova et al. 2024 for details).

## 4 RESULTS

### 4.1 Outflow detection rates

To obtain the [O III] outflow detection rate, which is the fraction of AGN that host an outflow out of each population, we calculate the number of AGN which showed signs of each category of outflow, [O III] fitted outflow, $W_{80}$ outflow, and $W_{80}$ likely outflow. As the matching process has inherent randomness, we calculate these fractions and bootstrap the uncertainties at the same time by re-performing the random $L_{6\,\mu m}$-$z$ matching 1000 times. This provides a more representative sampling of the data and its uncertainties. From the summation of these samplings, we calculate the mean value and its $1\sigma$ (16th and 84th percentiles) uncertainties for each of these fractions. These errors are displayed in Fig. 3.

Fig. 3 clearly shows that we see a higher outflow detection rate in radio detected AGN than radio non-detected AGN, with $> 3\sigma$ significance for AGN with a fitted [O III] outflow. Considering all outflow categories, 67.2 ± 3.4 per cent of radio detected AGN indicate signs of an outflow compared to just 44.6 ± 2.7 per cent of the radio non-detected AGN. If we consider only definite outflows within the [O III] fitted and $W_{80} > 800$ km s$^{-1}$ categories, the outflow detection rates are 55.3 ± 3.2 per cent for the radio detected AGN but 34.3 ± 2.3 per cent for the radio non-detected AGN. The outflow detection rates are displayed in Table 1.

**Table 1.** Outflow detection rates of the radio detected and radio non-detected populations, where [O III] fitted outflows have two components fitted to [O III], $W_{80}$ outflows have a single component and $W_{80} > 800$ km s$^{-1}$, $W_{80}$ likely outflows have a single component and 600 km s$^{-1}$ $< W_{80} <$ 800 km s$^{-1}$, and no outflows where a single component is fitted to [O III] with $W_{80} < 600$ km s$^{-1}$. AGN within the definite outflow category have an outflow classed as either a [O III] fitted outflow, or a $W_{80}$ outflow. AGN classed with a [O III] fitted outflow, $W_{80}$ outflow or $W_{80}$ likely outflow are consider in the all outflow category.

| | Radio detected | Radio non-detected |
|---|---|---|
| [O III] fitted outflow | 52.3 ± 2.8 | 34.3 ± 2.3 |
| $W_{80}$ outflow | 3.0 ± 1.6 | 0.0 ± 0.0 |
| $W_{80}$ likely outflow | 11.9 ± 1.1 | 10.3 ± 1.5 |
| All outflow categories | 67.2 ± 3.4 | 44.6 ± 2.7 |
| Definite outflows | 55.3 ± 3.2 | 34.3 ± 2.3 |
| No outflow | 32.8 ± 2.5 | 55.4 ± 2.4 |

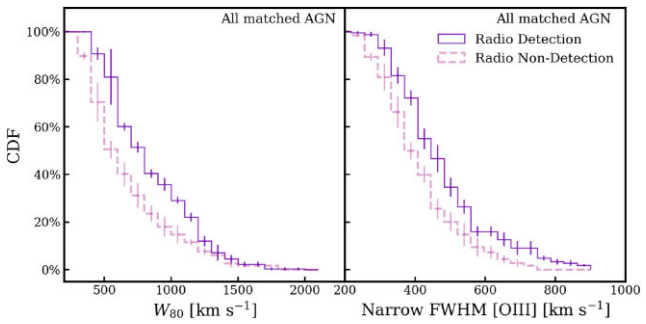


**Figure 4.** Average cumulative distribution functions of [O III] properties. The solid purple step function shows the distribution for the radio detected AGN and the dashed pink line shows the information from the radio non-detected sources. *Left:* average CDFs of $W_{80}$ [O III] showing the results from all 1000 matching iterations. *Right:* average CDFs of the FWHM of the narrow component of [O III] with the all matching iterations. Uncertainties are constructed using bootstrapping.

### 4.2 [O III] properties

To further understand the differences between [O III] from radio detected AGN and radio non-detected AGN, we plot the cumulative distribution functions (CDFs) of average emission line properties in Figs 4 and 5. As for the outflow detection rates, we use the 1000 matching runs to bootstrap the uncertainties. These CDFs encompass all 1000 matching runs. For the uncertainties, we bootstrap over all these 1000 matching runs to obtain a distribution of AGN for each bin. From these distributions we fit a Gaussian and take the standard deviation as the presented uncertainty of each bin.

Fig. 4 shows how the populations differ in $W_{80}$ and the FWHM of the narrow, or single Gaussian component fitted to [O III]. These CDFs contain all matched AGN. The CDF of $W_{80}$ (Fig. 4 left) shows us that the radio detected population has a significantly larger $W_{80}$ across the majority of the population than in the radio non-detected sample. The results change slightly when considering the AGN within the [O III] fitted outflow category, where radio detected AGN show a significantly larger $W_{80}$ at intermediate bins (see Appendix A for additional CDFs). We do point out, however that $W_{80}$ is a non-parametric measurement and is degenerate between the narrow and the broad components.

We check if the $W_{80}$ is dominated by one component by examining if there is a clear relationship between $W_{80}$ and either the broad or narrow components. There is a clear dependency only when a



Downloaded from https://academic.oup.com/mnras/article/536/2/1166/7911849 by Universiteit Leiden - LUMC user on 30 January 2026

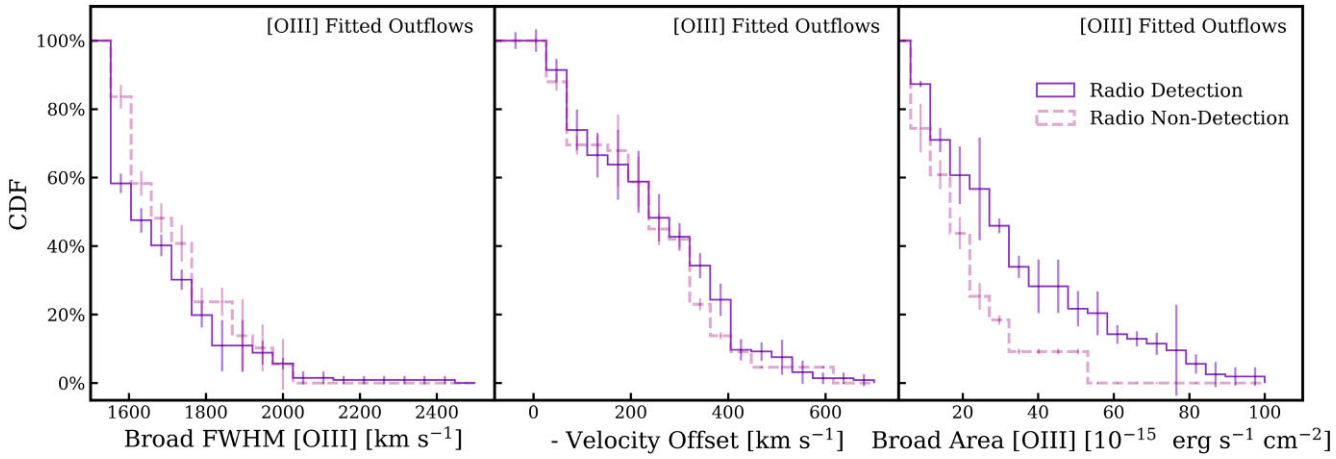


**Figure 5.** Further average cumulative distribution functions of [O III] properties. The solid purple step function shows the distribution for the radio detected AGN and the dashed pink line shows the information from the radio non-detected sources. All three panels have AGN with a second component fitted to [O III]. *Left:* CDF of the broad component of [O III] FWHM. *Middle:* negative velocity offset of the broad component relative to the narrow component. *Right:* area of the broad component, calculated using the peak and FWHM of the broad component. Uncertainties are constructed using bootstrapping.

single component is present, as expected. This is consistent with $W_{80}$ being a non-parametric measurement with degeneracies between two components when they are present.

The right panel in Fig. 4 presents the CDFs of the FWHM of the narrow, or single Gaussian component of the [O III] λ5007 emission line. It appears that radio detected AGN significantly dominate in the vast majority of bins when all matched AGN are considered. Radio detected AGN with two components fitted to [O III] still seem to dominate however at a lesser extent. For AGN with a single component fitted to [O III] the radio detected AGN appear to be very dominant within this category at all levels of FWHM (see Appendix A).

The left panel of Fig. 5 presents the CDF of the FWHM of the broad component which shows that radio non-detected AGN have a larger FWHM of the second component compared to the radio detected AGN until the highest FWHM where the distributions become equal within the uncertainties. This implies that if a second component is fitted to [O III], then this would be broader if the AGN does not have a detection in LoTSS.

The velocity offset CDF (middle panel in Fig. 5) shows us that the two populations have similar velocity offsets or blueshifts, aside from a few intermediate bins, where the radio detected AGN significantly dominate. We can therefore imagine that the two components in radio detected AGN would have similar separation as the two components in radio non-detected AGN.

Finally the right panel in Fig. 5 shows the CDF for the area of the broad component of [O III] for both the radio detected and radio non-detected populations. This area is calculated using both the peak and FWHM of the broad component. This CDF informs us that radio detected AGN have a brighter broad, second, component than radio non-detected AGN at a significant level for the majority of the bins.

One of the main differences we see in the CDFs between the two populations is the kinematics of the narrow, [O III] core component with the radio detected AGN having a larger FWHM. As we are most interested in the difference between the [O III] outflowing properties of the two populations, we produce a stack in Fig. 6 where we show the spectral fitting conducted to the median stacked spectra after we normalized spectra in the stack by the peak of the narrow component. The AGN contributing to these figures are from the closest matched population of the $L_{6\,\mu m}$ and redshift matching process. The left panel shows the results of the radio detected AGN and on the right, we see the radio non-detected AGN. We see that both the radio and radio non-detected AGN stacking results show that there appears to be an [O III] fitted outflow in both populations as a broad, second, component is fitted to both. It is interesting to note that from Fig. 6, we see an enhanced outflowing component in the normalized stack for the radio detected AGN. To quantify this, we calculate the area of just the broad component and find that the radio detected AGN have an outflowing component with an area of $204.74^{+17.97}_{-18.98}$ km$^2$ s$^{-2}$ compared to the radio non-detected AGN having an outflowing area of $173.91^{+17.74}_{-16.11}$ km$^2$ s$^{-2}$. We note that this result is not significant when considering the extremities of these uncertainties by $<5$ km$^2$ s$^{-2}$. As radio detected AGN show a brighter second component after normalization of the narrow component, this indicates that this is not a luminosity dependent affect because the ratio of the broad to the narrow component is larger for radio detected AGN than radio non-detected AGN, regardless of the brightness of the narrow component. From these stacks, we find the velocity offset is larger for the radio detected AGN, however if we consider the extremity of the uncertainties, this difference is not significant by $<3$ km s$^{-1}$.

Combining all the information from the CDFs and the stacked spectra, we can begin to build a picture of [O III] for typical radio and radio non-detected AGN. The [O III] λ5007 of radio detected AGN would appear to have a slightly broader, narrow component, but a narrower broad component than radio non-detected AGN, with a brighter broad component of [O III]. The distance between these two components would be similar for both populations.

### 4.3 Radio and [O III] luminosity relationship

In this section, we explore the relationship between radio and [O III] luminosity shown in Fig. 7. The left panel shows the [O III] λ5007 luminosity as a function of redshift. We bin our results in six redshift bins and take the median value of $z$ and $L_{[O\,III]}$ for the AGN in each bin. Other works conducted with similar redshift ranges are also shown (Liu et al. 2013; Rodríguez Zaurín et al. 2013; Harrison et al. 2014). Our sample has lower [O III] luminosities on average than these previous studies.

The right panel in Fig. 7 depicts the relationship between $L_{144\,MHz}$ and redshift with the $W_{80}$ of [O III] traced with a colour scale, with

Downloaded from https://academic.oup.com/mnras/article/536/2/1166/7911849 by Universiteit Leiden - LUMC user on 30 January 2026

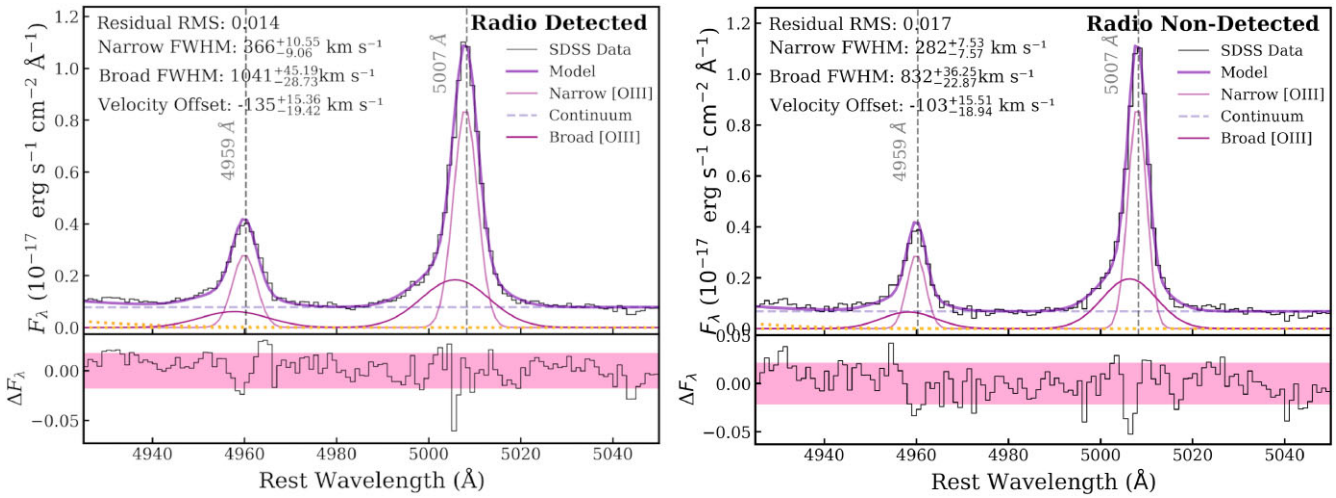


**Figure 6.** Composite spectra which are normalized by the peak of the narrow [O III] component and are produced from the closest matched $L_{6\,\mu m}$ and $z$ run, containing 59 AGN in each population with the MCMC fitting tool results applied. *Left:* radio detected AGN. *Right:* radio non-detected AGN. The bottom panel shows the residuals of the fits with $1\sigma$ of the residuals highlighted in the pink region. In the upper panel, the purple solid line shows the fit from the MCMC code to the SDSS data which are shown in black. The magenta line shows the broad component of [O III] with the pink Gaussians representing the narrow component of [O III].

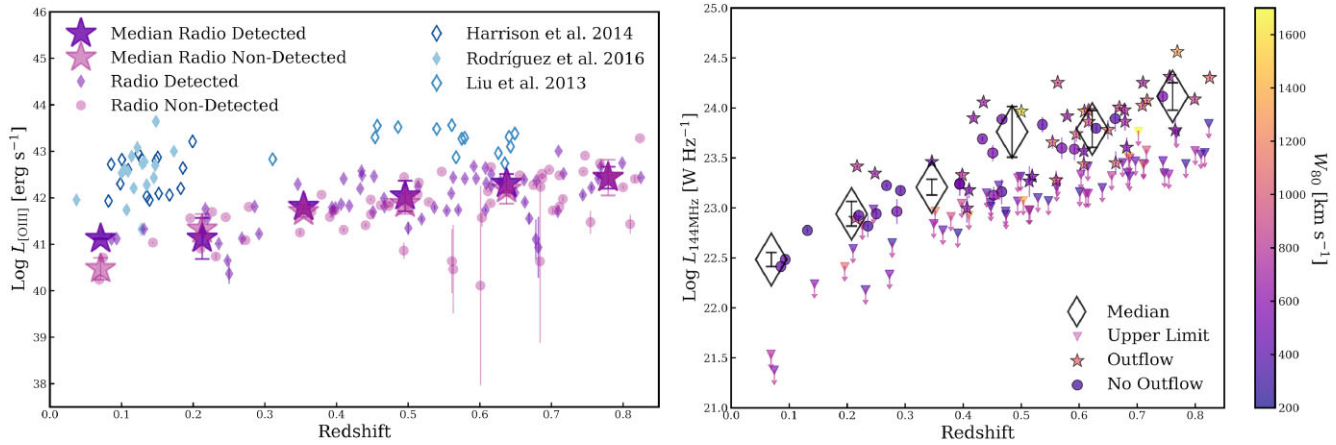


**Figure 7.** *Left:* total λ5007 Å $L_{[O\,III]}$ as a function of redshift. The star markers show the median values for six redshift bins, with purple indicating the median for the radio detected AGN, and pink for the radio non-detected AGN. The errors are the median absolute deviation. For the background sources, the purple diamonds show the radio detected population and the pink circles show the radio non-detected AGN. Similar studies are presented with various blue diamond markers. *Right:* relationship between $L_{144\,MHz}$ and redshift with the $W_{80}$ of [O III] traced with a colour map. Radio detected AGN are shown with either an outflow (small stars) or AGN with no outflow (circles). The median for five redshift bins are shown by large black hollow diamonds, with errors as the median absolute deviation. The upper limits for the radio non-detected AGN are shown by downward triangles.

$L_{144\,MHz}$ of the radio non-detected AGN being upper limits. We create five redshift bins and the median values of $L_{144\,MHz}$ for each bin are shown, with the median absolute deviation as the error.

The relationship between [O III] and radio luminosity was first presented in Rawlings et al. (1989). They discovered a positive correlation between the total $L_{[O\,III]}$ (both 5007 Å and 4959 Å) and $L_{178\,MHz}$. Fig. 8 shows $L_{144\,MHz}$ as a function of $L_{[O\,III]}$ (5007 Å only) with $W_{80}$ traced with a colour scale. Here, we see that as $L_{144\,MHz}$ increases, so does $L_{[O\,III]}$, which is to be expected and is in agreement with Rawlings et al. (1989). We note that our results show a Spearman rank correlation of 0.223, whereas Rawlings et al. (1989) present a value of 0.51. A value of zero indicates no association, while a value of unity indicated a strong association. We therefore find a weaker correlation than Rawlings et al. (1989). The difference may be due to Rawlings et al. (1989) using the total $L_{[O\,III]}$ while we use just λ5007 Å to calculate $L_{[O\,III]}$. Our results produce a best fit with a slope of 0.58. Rawlings et al. (1989) does not remove any relation that would be introduced by an AGN luminosity bias, however even after matching in $L_{144\,MHz}$ and redshift, we still see a correlation between [O III] and radio luminosity. We note that we can not determine if this relationship is real or due to the effect of the limited field of view and flux limits of our sample. To determine this we would require a larger sample.

### 4.4 Radio emission

#### *4.4.1 Radio excess*

To investigate the origin of the radio emission, we show the relationship between SFR and $L_{144\,MHz}$ in Fig. 9. Only radio detected sources are shown in this figure since Best et al. (2023) only carried



Downloaded from https://academic.oup.com/mnras/article/536/2/1166/7911849 by Universiteit Leiden - LUMC user on 30 January 2026

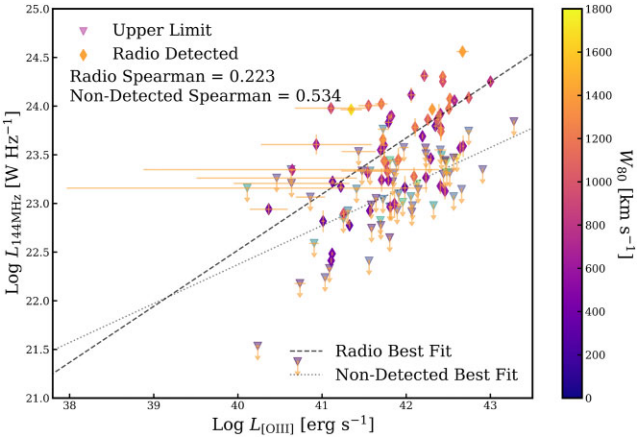


**Figure 8.** $L_{144\,\mathrm{MHz}}$ as a function of total $L_{[\mathrm{O\,III}]}$ with the $W_{80}$ traced by a colour scale. Radio detected AGN are plotted with diamonds and the upper limits for the radio non-detected AGN are shown by the downward triangles. The dashed black line show the best fit relationship for the radio detected AGN and the grey dotted line shows the best fit to the upper limits of the radio non-detected population.

out SED fitting to calculate the SFR for radio detected sources (see Section 2.1.1). We use the redshift presented in Best et al. (2023), which can be either spectroscopic or high quality photometric redshifts from Duncan et al. (2021), to calculate the radio luminosities to be consistent with their results. Overlaid we show our $L_{6\,\mu\mathrm{m}}$-$z$ matched sample.

On the left, we see the results for the sources within the Boötes field and on the right, we see the Lockman Hole and ELAIS-N1 sources. We show these fields separately as the scatter in the Boötes is slightly different, leading to an extra adjustment in this field. We show the SFR and $L_{144\,\mathrm{MHz}}$ relation found in Best et al. (2023) in both panels as well as the radio excess line which is 0.7 dex above the relation in Lockman Hole and ELAIS-N1. For Boötes an extra redshift dependent correction is necessary so the radio excess line is $0.7 + 0.1z$ above the relation, due to increased scatter in the SFR and $L_{144\,\mathrm{MHz}}$ relation for this field. Above these lines, sources are considered to be radio excess, where their radio emission is dominated by star formation. To guide the eye, we use the maximum redshift of our sample, $z = 0.83$, for the redshift dependent definition of radio excess in the Boötes field.

Only four sources from our sample appear to be radio excess as they lie above the radio excess divide, one in ELAIS-N1, three in Lockman, and none in Boötes. Two of the radio excess AGN have a broad, second component fitted to [O III]. Radio emission in sources above the radio excess line can be attributed to radio jets. The majority of our sample lies below the radio excess line, and we are unable to use this diagnostic to determine the origin of their radio emission.

#### *4.4.2 Radio morphology*

Radio morphology can help diagnose the source of radio emission, for example by identifying jets which can only be produced by AGN and not star formation. We study the radio morphology of the radio detected population at 6 arcsec which is available using the LoTSS catalogue. We visually classify the morphology of our sample. In all our 115 radio detected AGN, we find ∼93 per cent of sources (107/115) are unresolved, meaning only eight sources show resolved structure; two of these resolved AGN which lie within Boötes are shown in Fig. 10, five in Lockman, and one in ELAIS-N1. These unresolved source imply radio sizes less than 4.7 kpc.

For the majority of our sample, we therefore cannot use morphology to determine the source of the radio emission. This emphasizes the need for high resolution imaging to securely identify the radio morphology.

### 4.5 Comparison to other studies

The [O III] emission line kinematics in radio enhanced versus radio weak AGN were studied extensively by Mullaney et al. (2013). The authors show that AGN with $L_{1.4\mathrm{GHz}} > 10^{23}$ W Hz$^{-1}$ have a larger average FWHM than AGN with lower radio luminosities. In this large statistical sample, the authors use the flux-weighted average FWHM of the broad and narrow components whereas we study them separately. Although we have a smaller sample size, our study extends to lower radio luminosities (down to $L_{1.4\mathrm{GHz}} \sim 10^{20}$ W Hz$^{-1}$) and higher redshifts, and we match in $L_{6\,\mu\mathrm{m}}$ and redshift which may contribute to the seemingly different results we find. However, overall conclusions are still consistent: our sample is not dominated by powerful radio jets (Section 4.4.1), and we find differences in sources with strong versus weak radio emission (either radio detected versus not radio detected, this work; or $L_{1.4\mathrm{GHz}} > 10^{23}$ versus $L_{1.4\mathrm{GHz}} > 10^{23}$ W Hz$^{-1}$, Mullaney et al. 2013). To check the consistency of our samples we convert our $L_{144\,\mathrm{MHz}}$ to $L_{1.4\mathrm{GHz}}$ assuming a spectral index of 0.7 and split the radio detected sample into sources with $L_{1.4\mathrm{GHz}} > 10^{23}$ W Hz$^{-1}$ or $L_{1.4\mathrm{GHz}} < 10^{23}$ W Hz$^{-1}$ as well as removing sources that are above a redshift of 0.4 to match their selection. We then calculate the average FWHM as in equation (2) from Mullaney et al. (2013), and find the same trend for the average FWHM for low and high luminosity AGN (see fig. 9 in Mullaney et al. 2013).

Recently, Calistro Rivera et al. (2021, 2024) found that red quasars (which are known to be radio enhanced; Klindt et al. 2019) have a larger FWHM of the second component fitted to [O III] than their control quasars. It is difficult to draw a direct comparison between their work and ours because our sample spans the whole range of colours and the majority would not be classed as red quasars.

## 5 DISCUSSION

We see that radio detected AGN have a higher outflow detection rate compared to our radio non-detected population as well as differences in the kinematics of the [O III] emission line between the two populations. After normalizing for the narrow [O III] component, in the resulting stacked spectra we see that the radio detected AGN have a larger broad outflowing component than the radio non-detected AGN. This is suggestive of the radio detected AGN hosting outflows with a larger amount of gas than outflows produced by the radio non-detected population.

### 5.1 What is the origin of radio emission?

The SFR–$L_{144\,\mathrm{MHz}}$ relation has shown us that the majority of sources are not radio excess in both fields. Sources above the radio excess divide have radio emission which is likely to originate from a powerful jet. As only four AGN are above the radio excess divide, this shows that the radio emission is not driven by powerful radio jets. However, we can only rule out powerful jets as the dominant cause of the radio emission in this sample. The results of this paper also indicate that radio emission is produced when a large amount of ionized outflowing gas is present and here, we discuss two possible explanations as to why we see this. The possible mechanisms

Downloaded from https://academic.oup.com/mnras/article/536/2/1166/7911849 by Universiteit Leiden - LUMC user on 30 January 2026

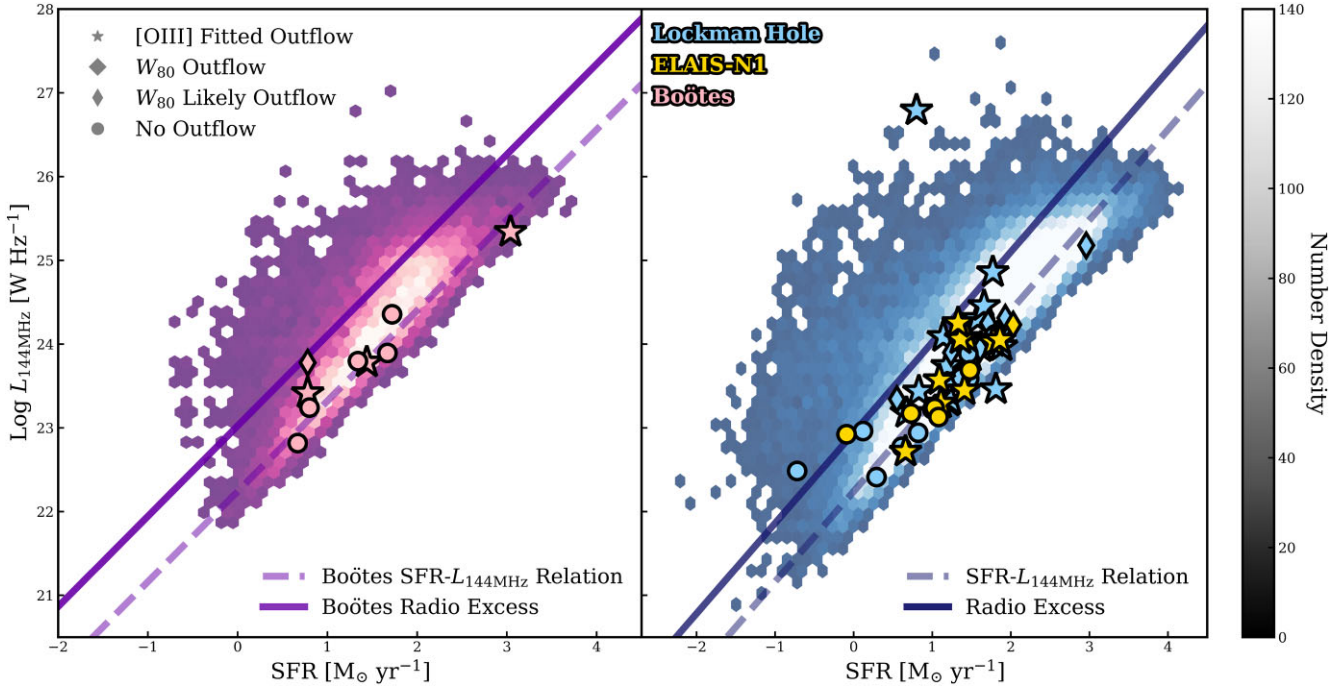


**Figure 9.** The relationship between SFR and $L_{144\,\mathrm{MHz}}$. The left subplot shows the result of the Boötes field (pink markers) and on the right Lockman Hole (blue markers) and ELAIS-N1 (yellow markers), the fields have been split because of the need for an extra adjustment to the radio excess in Boötes. Error bars are included but are too minimal to see. No upper limits are shown for the radio non-detected AGN because we do not have access for reliable SFR measurements for these AGN. The background hexagon bins show the distribution of sources with reliable SFR measurements with Boötes in purple and Lockman Hole and ELAIS-N1 combined in blue, where a hexagon is plotted for areas where there is four or more sources. On each panel, the faint dashed line shows the SFR–$L_{144\,\mathrm{MHz}}$ relation, which is the same for both fields. The solid line shows the radio excess divide which is 0.7 dex above the SFR–$L_{144\,\mathrm{MHz}}$ for Lockman Hole and ELAI-N1 with a slight redshift adjustment for Boötes. The over laid points with black edges are the sources within the best matched populations. The stars are sources with an [O III] fitted outflow, thick diamond host an $W_{80}$ outflow and thin diamonds are AGN with a likely outflow. Circles represent sources that show no indication of an outflow. The colour scale traces the number density of each hexagon and is shown as grey as the scale is the same for both subplots, hence it would be pink for Boötes and blue for Lockman Hole and ELAIS-N1.

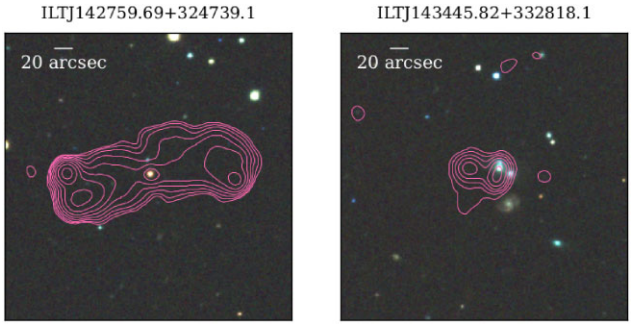


**Figure 10.** Cut outs (150 arcsec × 150 arcsec) of the only two resolved Boötes radio sources within our sample. We use the *g*, *r*, and *i* bands from SDSS to make a composite rgb optical image. The LoTSS radio contour plots are overlayed and the noise is set to 30 μJy (Tasse et al. 2021). The contour levels are $3\sigma$, $5\sigma$, $10\sigma$, $20\sigma$, and $40\sigma$.

responsible for the radio emission in this sample are star formation, small (weak) radio jets, or shocks associated with AGN winds.

Star formation is unlikely to be the driver of radio emission in our sample. We see that in radio detected AGN, there is a significantly larger amount of outflowing gas. Star formation is a relatively weak and widespread phenomenon in a galaxy, and therefore is unlikely to be the main driving mechanism for the increase in outflow gas.

Radio emission from low-power or small-scale jets would be directional, and have a particular geometric relationship with ionized outflows. If the radio jets are cospatial with the outflows, then it is possible the correlation between outflow detection rate and radio detection is due to orientation effects. In this scenario, the radio emission could be higher due to beaming in sources where outflows are along our line of sight. However, at the low frequencies of these observations, we expect beaming effects to be negligible. Small-scale jets can also explain the increased gas level as it could lead to more fuel for the AGN, and this fuel can possibly be launched as a radio jet later on in the AGN life cycle.

The alternative explanation is that AGN winds can be the main mechanism in producing radio emission in our sample. If the outflow is in the form of a wind then the higher level of gas would lead to the wind becoming more dense, and this increased density could cause a shock to occur within the wind and hence produce radio emission due to the particle acceleration within the shock front. This could explain the higher level of outflowing gas seen in radio detected AGN. Zakamska & Greene (2014) suggest that the driving mechanism is quasar winds that propagate into the ISM and produce shock fonts where particle acceleration occurs, hence producing radio emission. However, the authors also acknowledge that the radio and [O III] correlation could be driven by the mechanical energy of relativistic jets due to excessive heating releasing an ionized wind. The shocks suggested by Zakamska & Greene (2014) are not expected to produce radio emission causing sources to be radio excess. Nims, Quataert & Faucher-Giguère (2015) calculates that the synchrotron emission generated by shocks are about 5 per cent of the bolometric luminosity and in a later study Zakamska et al. (2016) investigates the kinematics



Downloaded from https://academic.oup.com/mnras/article/536/2/1166/7911849 by Universiteit Leiden - LUMC user on 30 January 2026

of [O III] of four extremely red quasars and estimates that at least 3 per cent of the bolometric luminosity is powering the kinematic energy of dusty winds. The addition of these to the radio emission from star formation is still well within the scatter of the SFR–$L_{144\,\mathrm{MHz}}$ relation, and the fact that a source is not radio excess does not rule out that AGN wind shocks are the cause of the radio emission. Therefore, high resolution follow-up will be crucial to determine the origin of this radio emission.

The driving mechanism linking radio emission and [O III] outflows is still up for debate. As already discussed, Zakamska & Greene (2014) suggest that utflows trigger shocks which drive the radio emission. More recently, Liao et al. (2024) studies the connection between $w_{90}$ of [O III] and radio emission from median stacked radio images from the Karl G. Jansky Very Large Array (VLA) Sky Survey (VLASS) (Lacy et al. 2020) from ∼37 000 radio quiet AGN. Similar to this work, the authors confirm a significant connection between [O III] and radio emission as well as suggesting the most likely explanation for the radio emission from their radio-quiet AGN is also AGN driven by either low-powered jets or winds.

Jarvis et al. (2019, 2021) follows-up around 40 radio-quiet AGN from Mullaney et al. (2013) with high frequency, high-resolution radio images from the VLA and enhanced Multi Element Remotely Linked Interferometer Network (e-MERLIN). These high-resolution images proved to be crucial to determining the origin of radio emission from this sample of radio-quiet AGN, where the authors found that the majority of the radio emission originates from radio jets with star formation likely to be responsible for ∼10 per cent of the radio emission. This highlights that high resolution imaging of our sample will be key to furthering our understanding of the radio emission from our sample of 198 AGN.

## 6 CONCLUSIONS

We form a sample of 198 AGN in the LoTSS Deep Fields, 115 of which are detected in LoTSS at 144MHz, and 83 with no detection. We use SDSS as a base sample and supplement the data with the deep multiwavelength information from the LoTSS Deep Fields. We match the radio non-detected to the radio detected AGN in $L_{6\,\mu\mathrm{m}}$ and redshift to remove any possible biases from AGN luminosity.

Using an MCMC statistical approach, we fit the [O III] emission line. We place each AGN in one of the four [O III] outflow subcategories: (i) [O III] fitted outflows, where two Gaussians are fitted to [O III]; (ii) $W_{80}$ outflow with one component fitted and $W_{80}>$ 800 km s$^{-1}$; (iii) $W_{80}$ likely outflows with one component fitted and 600 km s$^{-1}$ $< W_{80} <$ 800 km s$^{-1}$; and (iv) finally no outflow, where one component is fitted to [O III] and $W_{80} <$ 600 km s$^{-1}$.

In the radio detected population, we find 67.2 ± 3.4 per cent of these AGN show signs of an outflow occurring compared to just 44.6 ± 2.7 per cent of radio non-detected AGN. Even when we remove the $W_{80}$ outflow based subcategories, radio detected AGN still show a higher outflow detection rate. This indicates that [O III] outflows are more common in AGN where there is a detection in LoTSS compared to there being no detection present.

We use both stacked spectra and CDFs of the emission line parameters to understand the average profile of [O III] of the two populations. The CDFs tell us that radio detected AGN have a larger $W_{80}$ than the radio non-detected AGN as well as a broader, [O III] core component, however radio non-detected AGN have a broader, second component. To allow us to just study the differences between the outflowing component [O III], we produce stacks which have been normalized by the peak of the narrow component and find that radio detected AGN have a larger outflowing component with respects to the radio non-detected AGN, implying that more gas is present in [O III] outflows hosted by a radio detected AGN. This suggests radio emission from either low-powered jets or shocks from AGN driven winds.

We find that the majority of our radio detected sources are not radio excess. Therefore this radio emission appears not to originate from high-powered radio jets but is more likely from star formation, winds or low-powered radio jets.

To determine the origin of this radio emission from radio quiet AGN, we must study the radio morphology. However, we find that ∼93 per cent of sources within all three LoTSS Deep Fields are unresolved at 6 arcsec. By incorporating the international stations of LOFAR we can obtain sub-arcsec resolutions down to 0.3 arcsec which improves the resolution by a factor of 20. Using this subarcsec resolution imaging, which provides access to sub-galactic scales, we can use radio morphology and brightness temperature to determine the nature of AGN emission and separate it from radio emission due to star formation (Morabito et al. 2022). With this subarcsec resolution we will be able to study the morphology of previously unresolved sources. This will allow us to determine if the radio emission from these AGN is from the AGN activity or star formation.

The Lockman Hole Deep Field is the first wide-field image produced at sub-arcsec resolution with a frequency of $L_{144\,\mathrm{MHz}}$ (Sweijen et al. 2022). This process is very computationally heavy and took an estimated 250 000 core hours. A deeper image of ELAIS-N1, at the same resolution and frequency, combines four nights of observations, has also been released in de Jong et al. (2024). Using the same techniques, we are processing the Boötes Deep Field which will result in another wide-field image at sub-arcsec resolution at $L_{144\,\mathrm{MHz}}$. With these three data sets, we will be able to study their radio morphology and determine whether the radio emission is from AGN activity or star formation. This will lead us closer to understanding the nature of radio emission in radio quiet AGN.

## ACKNOWLEDGEMENTS

EE and LKM are grateful for support from the Medical Research Council (MR/T042842/1), CMH acknowledges funding from UKRI (UK Research and Innovation) (MR/V022830/1), MIA acknowledges support from the UK Science and Technology Facilities Council (STFC) studentship under the grant ST/V506709/1, RCH acknowledges support from NASA (National Aeronautics and Space Administration) through ADAP (Astrophysics Data Analysis Program) grant number 80NSSC23K0485, RK acknowledges support from the STFC via grant ST/V000594/1 and DJBS acknowledges support from the UK STFC under grant ST/V000624/1.

This paper is based on data obtained with the International LOFAR Telescope (ILT). LOFAR (Haarlem et al. 2013) is the Low Frequency Array designed and constructed by ASTRON. It has observing, data processing, and data storage facilities in several countries, that are owned by various parties (each with their own funding sources), and that are collectively operated by the ILT foundation under a joint scientific policy. The ILT resources have benefitted from the following recent major funding sources: CNRS-INSU, Observatoire de Paris and Université d'Orléans, France; BMBF, MIWF-NRW, MPG, Germany; Science Foundation Ireland (SFI), Department of Business, Enterprise and Innovation (DBEI), Ireland; NWO, the Netherlands; The Science and Technology Facilities Council, UK; Ministry of Science and Higher Education, Poland; The Istituto Nazionale di Astrofisica (INAF), Italy.

This research made use of the Dutch national e-infrastructure with support of the SURF Cooperative (e-infra 180169) and the

Downloaded from https://academic.oup.com/mnras/article/536/2/1166/7911849 by Universiteit Leiden - LUMC user on 30 January 2026

LOFAR e-infra group. The Jülich LOFAR Long Term Archive and the German LOFAR network are both coordinated and operated by the Jülich Supercomputing Centre (JSC), and computing resources on the supercomputer JUWELS at JSC were provided by the Gauss Centre for Supercomputing ev (grant CHTB00) through the John von Neumann Institute for Computing (NIC).

This work used the DiRAC at Durham facility managed by the Institute for Computational Cosmology on behalf of the STFC DiRAC HPC Facility (www.dirac.ac.uk). The equipment was funded by BEIS capital funding via STFC capital grants ST/P002293/1, ST/R002371/1, and ST/S002502/1, Durham University and STFC operations grant ST/R000832/1. DiRAC is part of the National e-Infrastructure.

## DATA AVAILABILITY

The target catalogue with derived properties of our sample will be available on CDS on publication. Spectral fitting results will be made available upon request.

The deep radio data used in this paper are from the LoTSS Deep Fields Data Release 1 which is presented in Tasse et al. (2021). The data are made publicly available through the LOFAR Surveys website (https://lofar-surveys.org/deepfields.html).

We use the SDSS Quasar catalogue from DR16 which can be accessed at https://www.sdss4.org/dr17/algorithms/qso_catalog/ and the broad-line AGN catalogue from SDSS DR7 which can be found at http://cdsarc.u-strasbg.fr/cgi-bin/ftp-index?/ftp/cats/J/ApJS/243/21.

The SDSS spectra used in the spectral fitting can be downloaded from https://dr14.sdss.org/optical/spectrum/search by uploading the source's location or plate information.

## REFERENCES

Aihara H. et al., 2018, PASJ, 70, S8
Alexander D. M., Hickox R. C., 2012, New Astron. Rev., 56, 93
Andonie C. et al., 2022, MNRAS, 517, 2577
Antonucci R., 1993, ARA&A, 31, 473
Arnaudova M. I. et al., 2024, MNRAS, 528, 4547
Ashby M. L. N. et al., 2009, ApJ, 701, 428
Ayubinia A., Woo J.-H., Rakshit S., Son D., 2023, ApJ, 954, 27
Best P. N. et al., 2023, MNRAS, 523, 1729
Birzan L., Rafferty D. A., McNamara B. R., Wise M. W., Nulsen P. E. J., 2004, ApJ, 607, 800
Bonzini M. et al., 2015, MNRAS, 453, 1079
Boroson T. A., Green R. F., 1992, ApJS, 80, 109
Bower R. G., Benson A. J., Malbon R., Helly J. C., Frenk C. S., Baugh C. M., Cole S., Lacey C. G., 2006, MNRAS, 370, 645
Brown M. J. I. et al., 2008, ApJ, 682, 937
Brown M. J. I., Dey A., Jannuzi B. T., Brand K., Benson A. J., Brodwin M., Croton D. J., Eisenhardt P. R., 2007, ApJ, 654, 858
Calistro Rivera G. et al., 2021, A&A, 649, A102
Calistro Rivera G. et al., 2024, A&A, 691, A191
Carnall A. C., 2017, SpectRes: a fast spectral resampling tool in Python. Available at: http://arxiv.org/abs/1705.05165
Carniani S. et al., 2015, A&A, 580, A102
Croton D. J. et al., 2006, MNRAS, 367, 864
de Jong J. M. G. H. J. et al., 2024, A&A, 689, A80
Delvecchio I. et al., 2017, A&A, 602, A3
Dimitrijević M. S., Popović L., Kovačević J., Dačić M., Ilić D., 2007, MNRAS, 374, 1181
Duncan K. J. et al., 2021, A&A, 648, A4
Fabian A. C., 2012, ARA&A, 50, 455
Fawcett V. A. et al., 2023, MNRAS, 525, 5575
Fitzpatrick E. L., 1999, PASP, 111, 63
Foreman-Mackey D., Hogg D. W., Lang D., Goodman J., 2013, PASP, 125, 306
Frey S., Paragi Z., An T., Gabányi K. E., 2012, MNRAS, 425, 1185
Gebhardt K. et al., 2000, ApJ, 539, L13
Girdhar A. et al., 2022, MNRAS, 512, 1608
Gitti M., Brighenti F., McNamara B. R., 2012, Adv. Astron., 2012, e950641
Gonzalez A. H. et al., 2010, in AAS May Meeting Abstracts #216. p. 415.13
Goodman J., Weare J., 2010, Commun. Appl. Math. Comput. Sci., 5, 65
Greene J. E., Ho L. C., 2005, ApJ, 627, 721
Greenwell C., Gandhi P., Stern D., Boorman P., Toba Y., Lansbury G., Mainieri V., Desira C., 2021, MNRAS, 503, L80
Haarlem M. P. v. et al., 2013, A&A, 556, A2
Harrison C. M., Alexander D. M., Mullaney J. R., Swinbank A. M., 2014, MNRAS, 441, 3306
Hinshaw G. et al., 2013, ApJS, 208, 19
Jannuzi B. T., Dey A., 1999, in Bunker A. J., van Breugel W. J. M., eds, ASP Conf. Ser. Vol. 193, The NOAO Deep Wide-Field Survey. Astron. Soc. Pac., San Francisco, p. 258
Jarvis M. E. et al., 2019, MNRAS, 485, 2710
Jarvis M. E. et al., 2021, MNRAS, 503, 1780
Kaiser N. et al., 2010, in Stepp L. M., Gilmozzi R., Hall H. J., eds, SPIE Conf. Ser. Vol. 7733, Ground-based and Airborne Telescopes III. SPIE, Bellingham, p. 77330E
Kakkad D. et al., 2020, A&A, 642, A147
Kellermann K. I., Sramek R., Schmidt M., Shaffer D. B., Green R., 1989, AJ, 98, 1195
Klein U., Lisenfeld U., Verley S., 2018, A&A, 611, A55
Klindt L., Alexander D. M., Rosario D. J., Lusso E., Fotopoulou S., 2019, MNRAS, 488, 3109
Kondapally R. et al., 2021, A&A, 648, A3
Kormendy J., Richstone D., 1992, ApJ, 393, 559
Kormendy J., Richstone D., 1995, ARA&A, 33, 581
Kukreti P., Morganti R., Tadhunter C., Santoro F., 2023, A&A, 674, A198
Lacy M. et al., 2020, PASP, 132, 035001
Lawrence A. et al., 2007, MNRAS, 379, 1599
Liao M., Wang J., Ren W., Zhou M., 2024, MNRAS, 528, 3696
Liu G., Zakamska N. L., Greene J. E., Nesvadba N. P. H., Liu X., 2013, MNRAS, 436, 2576
Liu H.-Y., Liu W.-J., Dong X.-B., Zhou H., Wang T., Lu H., Yuan W., 2019, ApJS, 243, 21
Lonsdale C. J. et al., 2003, PSAP, 115, 897
Lyke B. W. et al., 2020, ApJS, 250, 8
Macfarlane C. et al., 2021, MNRAS, 506, 5888
Magorrian J. et al., 1998, AJ, 115, 2285
Martin D. C. et al., 2005, ApJ, 619, L1
Mauduit J. C. et al., 2012, PASP, 124, 714
McNamara B. R., Nulsen P. E. J., 2012, New J. Phys., 14, 055023
Merritt D., Ferrarese L., 2001, ApJ, 547, 140
Morabito L. K. et al., 2022, A&A, 658, A1
Morrissey P. et al., 2007, ApJS, 173, 682
Mullaney J. R., Alexander D. M., Fine S., Goulding A. D., Harrison C. M., Hickox R. C., 2013, MNRAS, 433, 622
Nesvadba N. P. H., De Breuck C., Lehnert M. D., Best P. N., Collet C., 2017, A&A, 599, A123
Nims J., Quataert E., Faucher-Giguère C.-A., 2015, MNRAS, 447, 3612
Padovani P., Miller N., Kellermann K. I., Mainieri V., Rosati P., Tozzi P., 2011, ApJ, 740, 20
Panessa F., Baldi R. D., Laor A., Padovani P., Behar E., McHardy I., 2019, Nat. Astron., 3, 387
Park D., Barth A. J., Ho L. C., Laor A., 2022, ApJS, 258, 38
Petley J. W. et al., 2022, MNRAS, 515, 5159
Rawlings S., Saunders R., Eales S. A., Mackay C. D., 1989, MNRAS, 240, 701
Richards G. T. et al., 2006, ApJS, 166, 470
Rodríguez Zaurín J., Tadhunter C. N., Rose M., Holt J., 2013, MNRAS, 432, 138



Downloaded from https://academic.oup.com/mnras/article/536/2/1166/7911849 by Universiteit Leiden - LUMC user on 30 January 2026

Rosario D. J., Fawcett V. A., Klindt L., Alexander D. M., Morabito L. K., Fotopoulou S., Lusso E., Calistro Rivera G., 2020, MNRAS, 494, 3061
Sabater J. et al., 2021, A&A, 648, A2
Schinnerer E. et al., 2004, AJ, 128, 1974
Schinnerer E. et al., 2007, ApJS, 172, 46
Schlegel D. J., Finkbeiner D. P., Davis M., 1998, ApJ, 500, 525
Scholtz J. et al., 2020, MNRAS, 492, 3194
Scholtz J. et al., 2021, MNRAS, 505, 5469
Shimwell T. W. et al., 2017, A&A, 598, A104
Shimwell T. W. et al., 2019, A&A, 622, A1
Shimwell T. W. et al., 2022, A&A, 659, A1
Speranza G. et al., 2023, A&A, 681, A63
Sweijen F. et al., 2022, Nat. Astron., 6, 350
Tadhunter C., Tsvetanov Z., 1989, Nature, 341, 422
Tasse C. et al., 2021, A&A, 648, A1
Timmerman R. et al., 2022, A&A, 658, A5
Tsuzuki Y., Kawara K., Yoshii Y., Oyabu S., Tanabe T., Matsuoka Y., 2006, ApJ, 650, 57
Urry C. M., Padovani P., 1995, PASP, 107, 803
Véron-Cetty M.-P., Joly M., Véron P., 2004, A&A, 417, 515
Villar-Martín M., Binette L., Fosbury R. A. E., 1999, A&A, 346, 7
Webster B., Croston J. H., Harwood J. J., Baldi R. D., Hardcastle M. J., Mingo B., Röttgering H. J. A., 2021, MNRAS, 508, 5972
Werner M. W. et al., 2004, ApJS, 154, 1
White S. V., Jarvis M. J., Häußler B., Maddox N., 2015, MNRAS, 448, 2665
Woo J.-H., Bae H.-J., Son D., Karouzos M., 2016, ApJ, 817, 108
Yue B.-H. et al., 2024, MNRAS, 529, 3939
Zakamska N. L. et al., 2016, MNRAS, 459, 3144
Zakamska N. L., Greene J. E., 2014, MNRAS, 442, 784
Zhou H., Wang T., Zhang X., Dong X., Li C., 2004, ApJ, 604, L33

## APPENDIX

Here, we present additional CDFs to support the discussion in Section 4.2 to further demonstrate how the [O III] line profiles differ in the radio detected AGN compared to the radio non-detected AGN. The top panels of Fig. A1 show the results for the CDFs of $W_{80}$ for AGN with [O III] fitted outflows (upper left) and AGN with only a single component fitted to [O III] (upper right). The lower two panels show the CDFs for the FWHM of the narrow component, with the lower left panel containing AGN with an [O III] fitted outflow and the lower right panel containing AGN with no broad component, so only a narrow component is fitted to [O III].

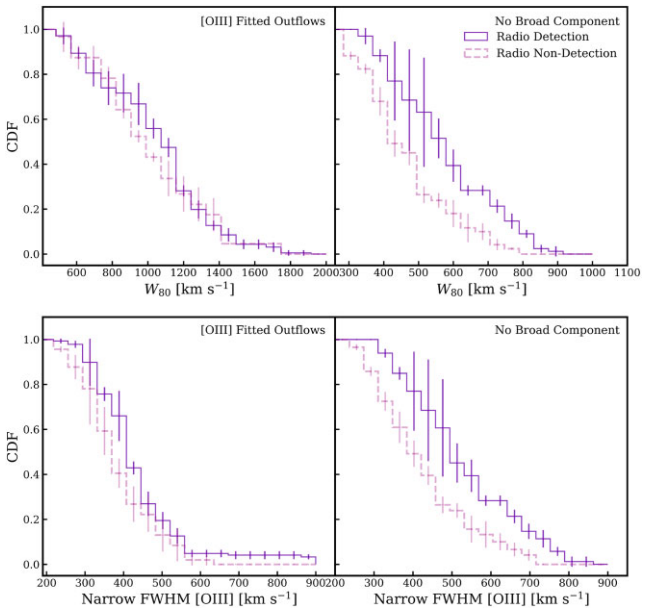


**Figure A1.** Further average cumulative distribution functions of [O III] properties. The solid purple step function shows the distribution for the radio detected AGN and the dashed pink line shows the information from the radio non-detected sources. *Upper left:* CDFs of $W_{80}$ [O III] showing the results only AGN which are fitted with a second component. *Upper right:* CDFs of $W_{80}$ [O III], all AGN which are fitted with a single Gaussian. *Lower left:* CDFs of the FWHM of the narrow component of [O III] with only AGN which are fitted with a second component. *Lower right:* CDFs of the FWHM of the narrow component of [O III] with all AGN which are fitted with a single Gaussian. The uncertainties presented are as a result of bootstrapping.

This paper has been typeset from a TEX/LATEX file prepared by the author.

Downloaded from https://academic.oup.com/mnras/article/536/2/1166/7911849 by Universiteit Leiden - LUMC user on 30 January 2026

© 2024 The Author(s).
Published by Oxford University Press on behalf of Royal Astronomical Society. This is an Open Access article distributed under the terms of the Creative Commons Attribution License (https://creativecommons.org/licenses/by/4.0/), which permits unrestricted reuse, distribution, and reproduction in any medium, provided the original work is properly cited.